A Shallow Shock: The 25 February 2019 M_L 4.9 Earthquake in the Weiyuan Shale Gas Field in Sichuan, China

Hongfeng Yang[*1], Pengcheng Zhou[1], Nan Fang[2,3], Gaohua Zhu[1], Wenbin Xu[2,3], Jinrong Su[4], Fanbao Meng[1], and Risheng Chu[5]

Abstract

Earthquakes rarely occur at extremely shallow depths, for example, less than 2 km. Even for induced earthquakes that are typically shallower than tectonic events, only very small ones have been reported in such depths. The M_L 4.9 earthquake (M_w 4.3) that struck the Rongxian County, Sichuan, China on 25 February 2019 was an extremely shallow event. Seismological and geodetic data constrained the mainshock depth at ∼ 1 km with a thrust-faulting mechanism, consistent with the Molin fault orienting northwest. Two foreshocks with magnitudes larger than 4 occurred on an unmapped fault striking northeast, right next to an injection well where hydraulic fracturing (HF) was conducted. The focal depths of the two foreshocks were at ∼ 2.7 km, coinciding with the depth of HF. Coulomb failure stresses of the two foreshocks on the Molin fault was ∼ 3 kPa, smaller than typical static triggering threshold (10 kPa), and thus their triggering effects were mild. As the fault was hydraulically sealed from HF, we suggested that the M_L 4.9 earthquake was possibly triggered by nearby HF activities through poroelastic stress transfer. Such findings held significant implications for shale gas development by considering seismic hazard associated with shallow faults.

Introduction

It was well known that anthropogenic processes can trigger earthquakes large enough to harm infrastructure and people (Ellsworth, 2013; Grigoli *et al.*, 2017; Yang *et al.*, 2017). In particular, recent heightened concern had been raised in a number of places where unconventional energy production took place, such as geothermal development (Grigoli *et al.*, 2018; Kim *et al.*, 2018), shale gas production (Clarke *et al.*, 2014; Atkinson *et al.*, 2016; Bao and Eaton, 2016), underground gas storage (Zhou *et al.*, 2019; Jiang *et al.*, 2020), and so on. The mechanisms to induce earthquakes were commonly attributed to pore-pressure perturbation or poroelastic stress changes by the bulk deformation of rock matrix, depending on whether the faults were hydraulically connected to the fluid reservoir (Ellsworth, 2013). Recently, injection-induced aseismic slip propagating into seismogenic portion of the faults (Bhattacharya and Viesca, 2019; Eyre *et al.*, 2019) and cascading triggering effects by small earthquakes (Brown and Ge, 2018) had been suggested to play significant roles in earthquakes caused by fluid injection.

Hydraulic fracturing (HF), also termed fracking, had been extensively used to extract resources from unconventional reservoir such as low-permeability shale rocks. Accompanying HF, numerous earthquakes with moment magnitudes (M_w) less than 0 were induced, which were valuable to monitor fracture growth. However, damaging earthquakes with $M_w > 4$ triggered by HF had been reported recently, with notable examples in North America (Babaie Mahani *et al.*, 2019; Wang, Harrington, *et al.*, 2020), United Kingdom (Eyre *et al.*, 2019), and China (Lei *et al.*, 2017; Meng *et al.*, 2019). In the literature, "induced" and "triggered" sometimes were mixed. Here, we followed the convention in Ellsworth *et al.* (2019), in which "induced earthquakes" referred to events with magnitudes consistent with the spatial dimension of anthropogenic activities, whereas "triggered earthquakes" denoted runaway ruptures, although the ruptures may have nucleated within the rock volume perturbed by industrial activities. By far, the largest HF triggered earthquake (the 2018 Xingwen earthquake with a local magnitude M_L 5.7) occurred in the southern Sichuan basin (Lei *et al.*, 2019a), where the Changning–Weiyuan shale gas block (Fig. 1a) had been
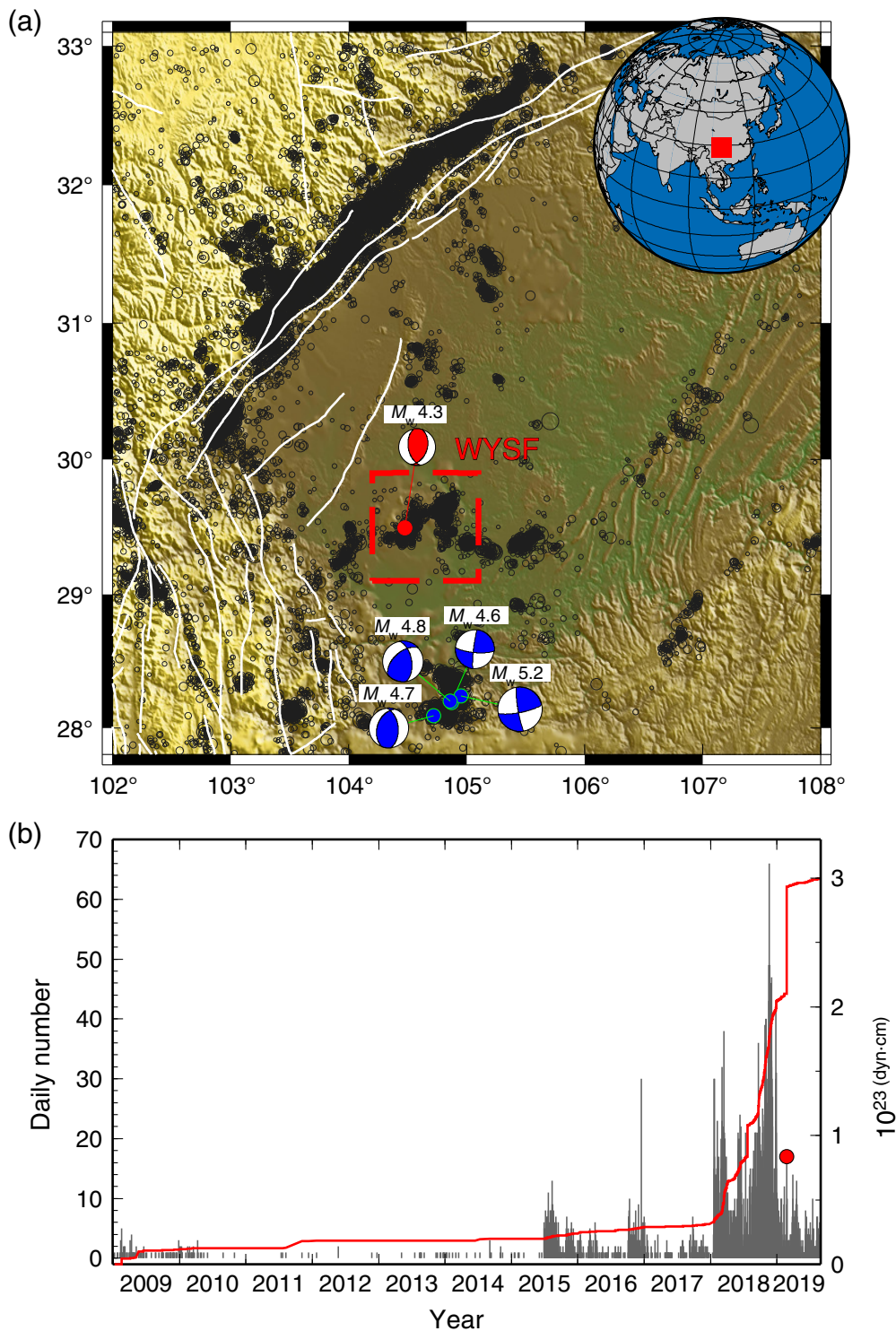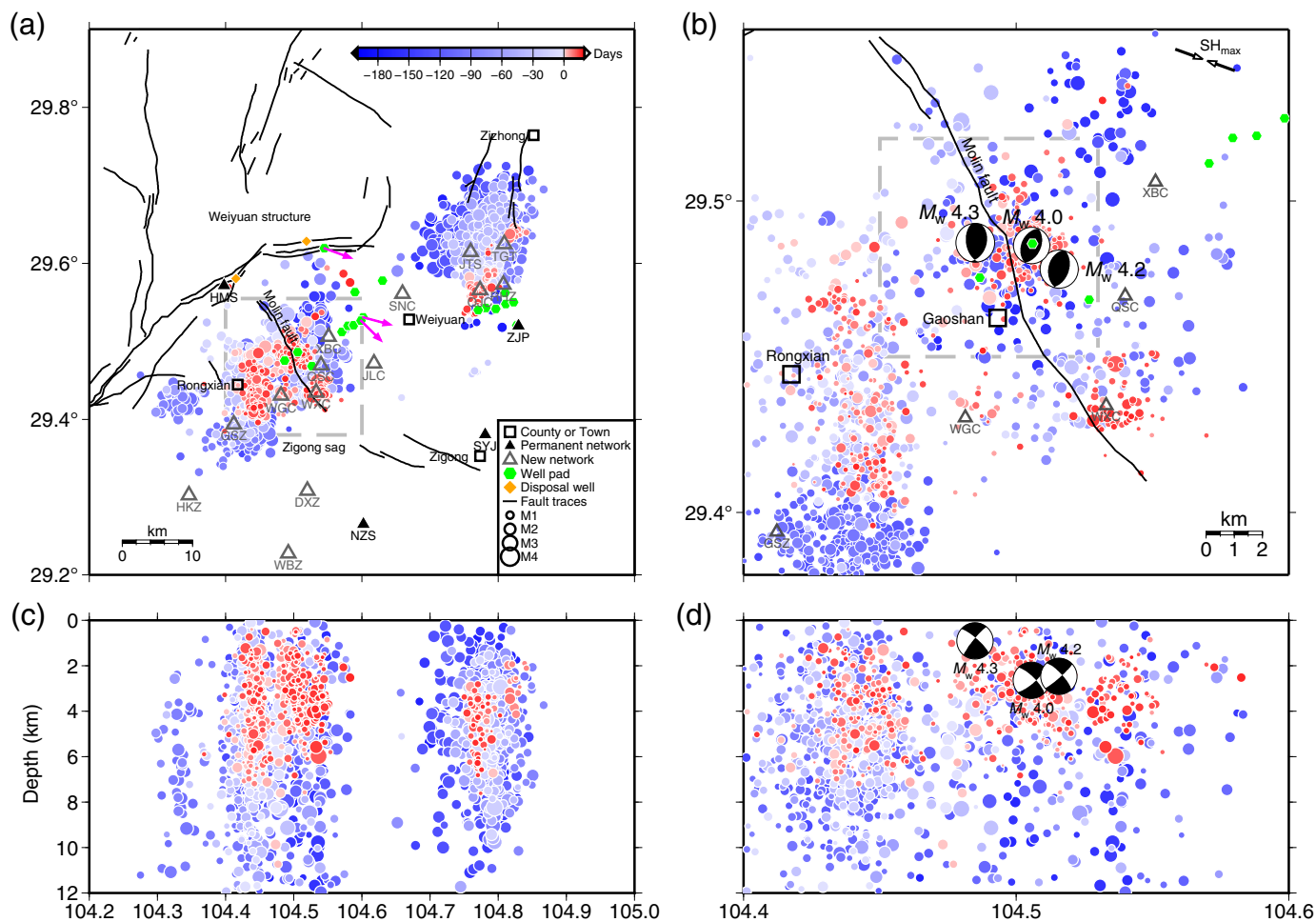
Figure 1. Surging earthquakes in the Sichuan basin. (a) Seismicity with local magnitudes larger than 1 since December 2008 are shown by black circles. White lines represent mapped faults. Blue focal mechanism plots denote moment tensor solutions of induced earthquakes in the Changning region (Lei *et al.*, 2017, 2019a). Red focal mechanism plot indicates the 25 February 2019 M_w 4.3 (M_L 4.9) earthquake. WYSF, Weiyuan shale gas field. Inset shows the location of the study region. (b) Daily number of earthquakes ($M_L > 1$) in the Rongxian–Weiyuan region with location shown in (a) by the red dashed lines. Red line denotes seismic moment release (converted from $M_L = 1.3 M_w - 0.88$ that was empirically estimated in the region) from December 2008 to March 2019. Red dot marks the occurrence time of the 25 February 2019 mainshock. The color version of this figure is available only in the electronic edition.

discovered and developed since 2011. A few other $M_w > 4$ earthquakes had been linked with HF in the Changning shale gas block, including five M_L 4–5 earthquakes in 2017 (Lei *et al.*, 2017; Meng *et al.*, 2019) and an M_L 5.3 earthquake in 2019 (Lei *et al.*, 2019a). In addition to HF triggered earthquakes, fluid injection for salt mining in the Changning area had been conducted for three decades, which possibly led to an M_w 6.0 earthquake in June 2019 (Lei *et al.*, 2019b).

In contrast, the Rongxian–Weiyuan region, located ~150 km north of Changning, had infrequent seismicity with M_L larger than 1 before mid-2015 (Fig. 1b). Then, earthquakes occurred more often, but the magnitudes were up to M_w 3.4 before 2018 (Lei *et al.*, 2017). The number of earthquakes with $M_L > 1$ increased drastically from 2018, with a few $M_L > 4$ damaging events (Fig. 1b). On 25 February 2019, an M_L 4.9 earthquake struck the region at 1:15 p.m., with a reported intensity of VI. As reported by *The Paper*, the earthquake caused two fatalities in the Gaoshan Town and 12 injuries, resulting in numerous damaged houses, and an estimated economic loss of 14 million RMB (~2 million U.S.). The earthquake was preceded by two **M** 4+ foreshocks, one at 5:38 p.m. on 24 February and the other at 8:40 a.m. on 25 February. HF wells within 2 km to their epicenters were in operation, before the occurrences of these earthquakes. Immediately after the mainshock, HF activities in the Rongxian County were shut down. Identifying the responsible faults of the

Figure 2. Relocated earthquakes and focal mechanisms.
(a) Mapped faults (black lines), local seismic stations (black and gray triangles), and relocated earthquakes (color dots) with colors showing their occurrence time relative to the origin time of the mainshock. Green hexagons denote locations of hydraulic fracturing wells. Purple arrows show directions of maximum horizontal stress from borehole measurements. (b) Dashed gray lines denote the area, a zoom-in map showing earthquake locations and moment tensor solutions of the three **M** 4+ earthquakes. (c) and (d) Depth view of the relocated earthquakes corresponding to (a) and (b), respectively. The color version of this figure is available only in the electronic edition.

earthquakes and finding the potential link with HF are critical not only for seismic hazard assessment in the region, but also for sustainable development of shale gas industry in China.

To infer which mechanism could have triggered earthquakes, source parameters of earthquakes, including focal depths, as well as states of hydraulic connection between injection and source faults were critical. In this study, we conducted high-resolution relocations of the February 2019 Rongxian–Weiyuan earthquake sequence, obtained focal mechanisms of the largest earthquakes using local and regional seismic network data, and derived the rupture dimension of the mainshock from Interferometric Synthetic Aperture Radar (InSAR) observations. We also calculated the Coulomb failure stress (CFS) caused by the two foreshocks on the fault plane of the mainshock to investigate their causal link. The well-constrained source depths and spatiotemporal distribution of earthquakes provided valuable information to identify the seismogenic faults and to understand how the earthquakes occurred.

Geologic Settings and Shale Gas Production

The Weiyuan shale gas block is located in the Weiyuan–Rongxian Counties and Zizhong City in the Sichuan Province, neighboring the Longquan Mountain structural belt

in the west, central Sichuan monocline in the north, and the Zigong sag in the south (Wei *et al.*, 2008). The local geology is characterized by the Weiyuan anticline, a northeast–southwest-trending dome structure, with many mapped faults trending in the northeast direction on the north flank, and several faults (e.g., Molin fault) trending in the southeast direction on the south flank (Fig. 2a). Based on geological survey, the Molin fault was mapped as a reverse fault dipping to the west, extending ∼15 km along strike (Wei *et al.*, 2008). On seismic reflection profiles near the epicenter of the 2019 February earthquake, the Molin fault was found to extend to and

terminate at the detachment interface dated middle Triassic, ~1.5 km in depth (Wang, Yang, et al., 2020). The maximum horizontal stress ($S_{H\,max}$) orientation near the Molin fault was measured at boreholes Wei201 and Wei202, around 105°–135° (Fig. 2a; Ma et al., 2017). No earthquakes larger than M_L 3 were found near the fault before 2019 (Fig. S1, available in the supplemental material to this article). Indeed, historical earthquakes in the region were sparse, with five $M_L > 4$ earthquakes within 50 km of the 2019 mainshock between 1970 and 2018. Among them, the largest earthquake was the **M** 4.8 earthquake on 29 March 1985, ~50 km to the mainshock. However, frequent $M_L > 1$ earthquakes had been observed in the Weiyuan shale gas block since 2014 (Fig. 1b), especially in the Rongxian County since 2018 (Lei et al., 2019a).

The Rongxian–Weiyuan region is covered by the upper Ordovician Wufeng Formation to lower Silurian Longmaxi Shale Formation at depths of 1.5–4.5 km (Wu et al., 2019). The Longmaxi–Wufeng formations, with an average thickness of 35–40 m in good quality for production, had been demonstrated with resourceful shale gas and thus were primarily targeted for shale gas production. The Weiyuan shale gas reservoir was one of high-productivity shale gas fields, with a target production volume of 2 billion m³ shale gas by 2015, nearly one-third of the total target in China. The "Wei-201 Well," located at the Laochang Village, Xinchang Town, Weiyuan County, became the first shale gas well in China in 2010 (Fig. 2a).

Since 2010, numerous fracking wells had been drilled in the Rongxian–Weiyuan region. However, there were no direct online resources listing the well locations. Because drilling wells and conducting relevant construction required approvals from local and provincial governments, we had then searched for the approval reports of the fracking wells in the Rongxian–Weiyuan region, with online sources from the government website (see Data and Resources). We compiled a list of well locations that had approval time before 2019. Since 2018, at least 48 horizontal well drillings had been projected on 13 well pads (six in the Gaoshan Town; Fig. 2), with average injection depth of ~3.4 km and horizontal well branches extending ~1.7 km. In the vicinity of the Gaoshan Town, where the mainshock intensity was VI, three of six HF well pads (drilled or operated) were located within distances of 0.5–2 km to the Molin fault (Fig. 2b). Unfortunately, no data of injection time, volume, and rate were available to public.

Seismic Network and Velocity Models
To locate the earthquakes, we used three regional 1D velocity models. The first was derived from active source refraction profiles and body-wave arrival times of earthquakes in the Sichuan basin and surrounding regions (Zhao et al., 1997). The second one is based on a V_S model derived from ambient-noise tomography in adjacent regions (Wang et al., 2013) and an assumed $V_P/V_S = 1.73$ (Lei et al., 2017). To constrain the moment tensor solutions of the largest earthquakes, we
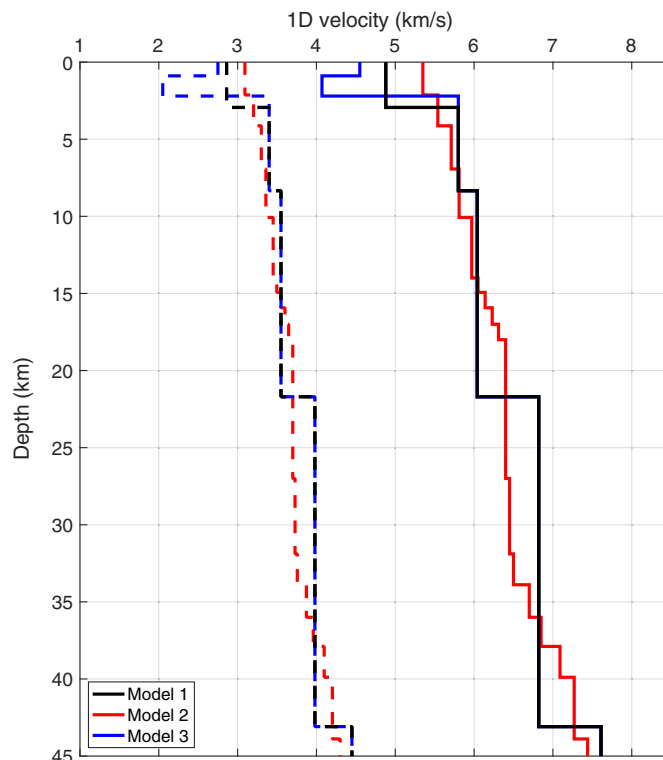

Figure 3. P- and S-wave velocity model constructed in this study. Model 1 (Zhao et al., 1997), model 2 (Lei et al., 2017), and model 3 (modified from Zhao et al., 1997; Meng et al., 2018). The color version of this figure is available only in the electronic edition.

constructed a local velocity model (Fig. 3) based on the 1D regional velocity model (Zhao et al., 1997) for depths greater than 3 km. At shallower depth, we adopted the velocity from well-logging data obtained in the Weiyuan shale gas field (Meng et al., 2018), which indicated a low-velocity layer below 1 km (Fig. 3). The effects of velocity models on source parameters will be discussed later.

To derive source parameters of the 2019 Rongxian earthquake sequence, we used all available local and regional stations (Fig. S2), including the permanent seismic network in Sichuan and some local seismic networks such as Zigong, Yibin, and Weiyuan stations. There are more than 10 stations as close as 10–20 km in our study area, with the nearest station (HMS) to the mainshock at a distance of ~15 km. After the mainshock, a temporary seismic network had been deployed since 28 February 2019 (Fig. 2), which was helpful to locate some aftershocks. Catalog data from 1 September 2018 to 13 March 2019 were collected from the China Earthquake Data Center, bounded by longitudes 104.2° and 105° and latitudes 29.3° and 29.8°. P and S travel times on nearby seismic stations were obtained from the Sichuan Earthquake Agency. Waveform data of the largest earthquakes were obtained from Data Management Centre of China National Seismic Network at Institute of Geophysics, China Earthquake Administration (Zheng et al., 2010).

TABLE 1

Double-Couple Moment Tensor Solutions of the Largest Four Earthquakes

Event Time	M_L	Strike/Dip/Slip (°)	M_w	Depth (km)
2019/02/23 21:38:08	4.7	FM1 190/42/83	4.2	2.6
		FM2 19/48/96		
2019/02/25 00:40:26	4.3	FM1 202/43/90	4.0	2.9
		FM2 22/47/90		
2019/02/25 05:15:58	4.9	FM1 170/51/72	4.3	1.0
		FM2 17/42/11		
2019/03/08 11:14:30	3.2	FM1 179/60/82	3.5	2.0
		FM2 15/31/104		
2019/02/14 to 2019/02/28 (InSAR analysis)	NA	FM1 170/42/90	4.4	$1.33^{+0.95}_{-0.55}$
		FM2 350/48/90		

InSAR, Interferometric Synthetic Aperture Radar.

Results
Seismological constraints on the earthquake sequence

We first relocated these earthquakes by the double-difference method (Waldhauser and Ellsworth, 2000), using our constructed velocity model (model 3 in Fig. 3). After relocation, uncertainties of most earthquake locations were less than 500 m in horizontal distances and 1 km at depth (Fig. S3). We also conducted tests on effects of uncertainties in velocity models on earthquake locations. Using different velocity models (Zhao *et al.*, 1997; Lei *et al.*, 2017), we found that horizontal and vertical location uncertainties were on the same order with those using velocity model 3. Although spatial pattern of seismicity distribution was similar among the three velocity models, depth distribution was certainly affected even for aftershocks that were recorded by newly deployed temporary network (red circles in Fig. S4). For the three **M** 4+ earthquakes, uncertainties caused by different velocity models were ∼1 km in depth and less than 100 m in epicentral locations (Fig. S4).

After relocation, most earthquakes distributed in two clusters, one around the Rongxian County and the other one between the Weiyuan County and the Zizhong City (Fig. 2a), but they did not necessarily correlate with mapped faults. The two **M** 4+ foreshocks were located in the east of the Molin fault, whereas the mainshock was located ∼1 km west to the Molin fault (Fig. 2b). Most earthquakes in the Rongxian cluster occurred in depths of 2–8 km (Fig. 2c,d).

We then derived focal mechanism solutions for the largest earthquakes using the generalized cut-and-paste method (Zhu and Helmberger, 1996; Zhu and Ben-Zion, 2013). Using the newly constructed 1D velocity model (model 3), we computed the Green's functions using a Haskell propagator matrix method (Zhu and Rivera, 2002). The original seismograms were filtered with frequency band of (0.05, 0.15) Hz for the smaller earthquakes and (0.03, 0.1) Hz for the mainshock. Full moment tensors were then obtained by a grid search with respect to the moment magnitude and strike, dip, and slip angles of the faults, as well as the compensated linear vector dipole (CLVD) component. In comparison, we also derived pure double-couple (DC) solutions, which were listed in Table 1.

According to the DC solution, the mainshock had a moment magnitude of 4.3 and occurred on a thrust fault orienting 170°, dipping to the west with a dip angle of 52° (Fig. 2b), which is consistent with the fault geometry shown in reflection profiles (Wang, Yang, *et al.*, 2020). In the full moment tensor solution, the fault orientation (179°) and dip angle (46°) were close to those in the DC solution, and the CLVD component accounted 13% (Fig. 4a). Apparently, there was a trade-off between the fault geometry and the CLVD component. The focal depth was ∼1 km in both the solutions (Fig. 4b,c). We also tested the effects of different velocity models (Fig. 3) and found that they did not impact the moment tensor solutions and focal depth (Fig. 4e,f). The location and focal mechanism solution suggested that the mainshock occurred on the northwest-trending Molin fault.

The two **M** 4+ foreshocks exhibited nearly identical thrust-faulting mechanisms (Fig. 2b), with orientations along northeast ∼10°. Compared with the shallow mainshock (1 km), the two foreshocks were consistently located at greater depths, 2–3 km, using different velocity models (Fig. S5). The CLVD components of the two foreshocks were both minor, 2% and 5%. The optimal depth was ∼2.7 km, coinciding with
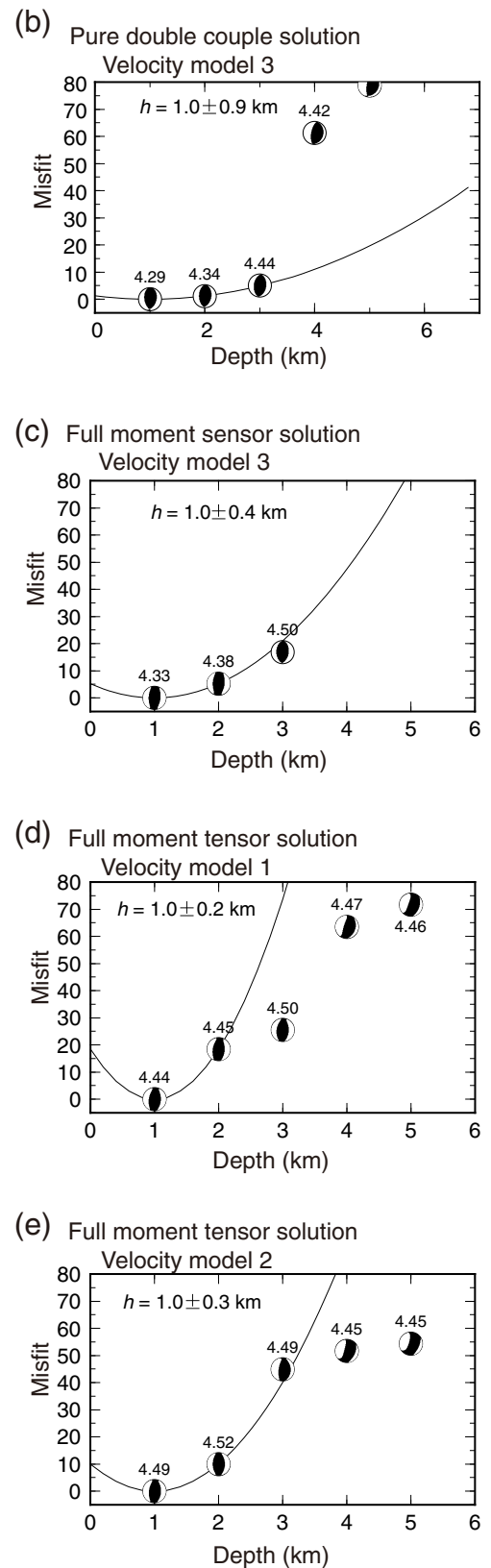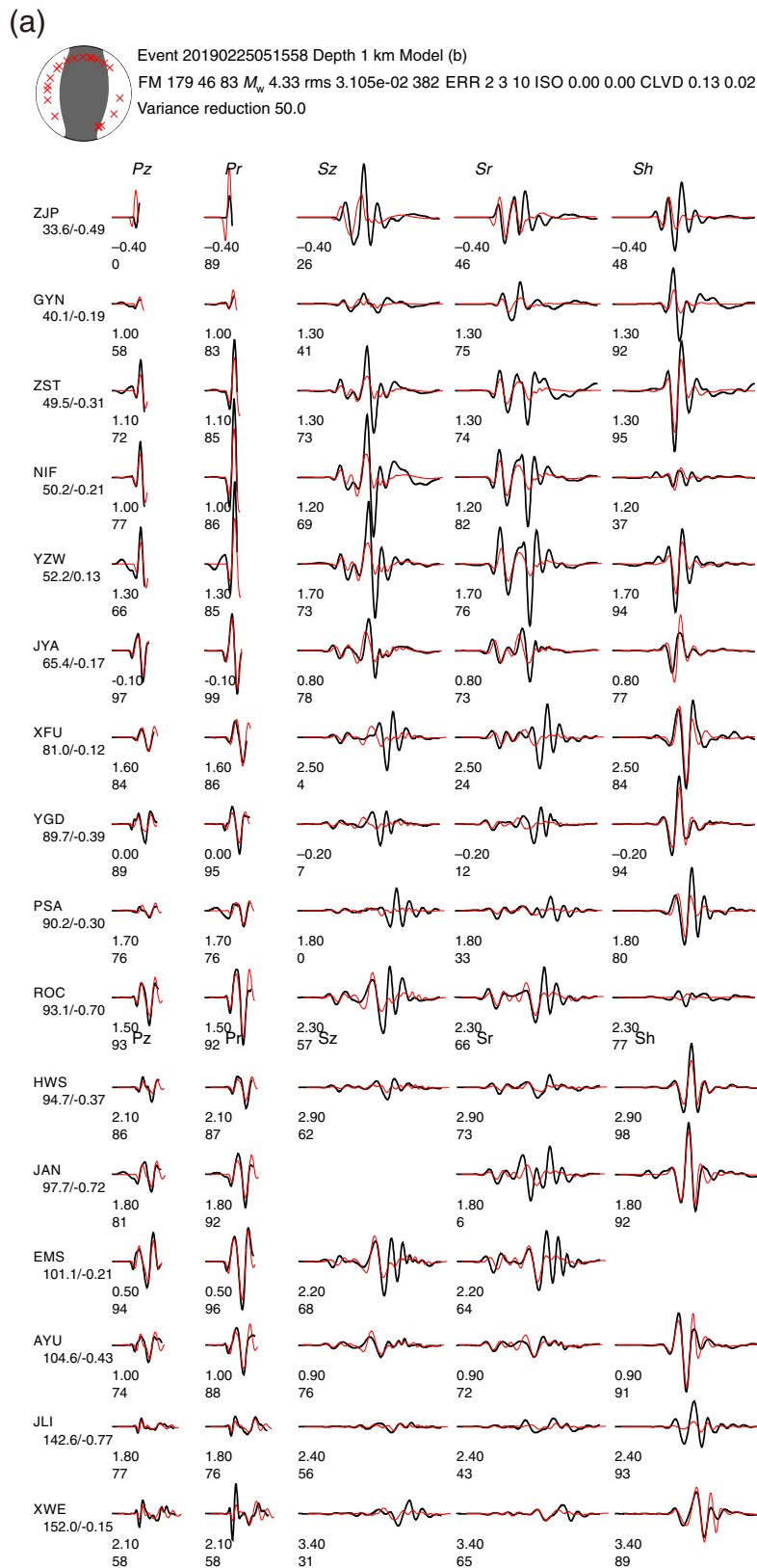
Figure 4. (a) Waveform fit of the best full moment tensor solution for the mainshock. Depth sensitivity tests on different velocity models of moment tensor solutions: (b) pure double-couple solution and (c) full moment tensor solutions using model 3 in Figure 3, (d) full moment tensor solutions using model 1 (Zhao *et al.*, 1997), and (e) model 2 (Lei *et al.*, 2017). CLVD, compensated linear vector dipole; ERR, error; FM, focal mechanism solution; ISO, isotropic component; rms, root mean square. The color version of this figure is available only in the electronic edition.
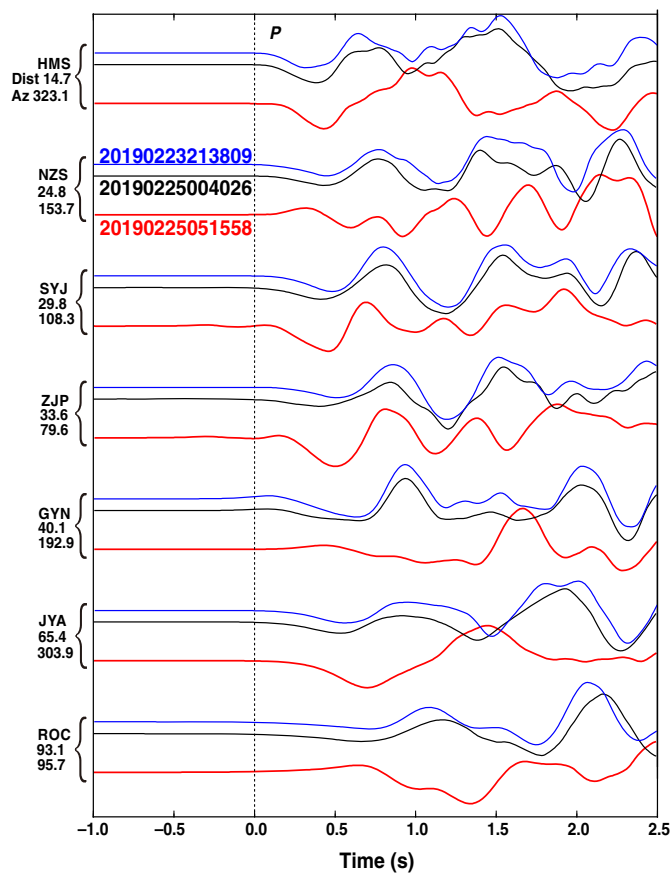
Figure 5. Waveform comparison of the mainshock (red) and the two **M** 4 foreshocks (blue and black) at station across different distances (km) and azimuths, shown on left. All waveforms were aligned by our manually picked *P*-wave arrivals. The color version of this figure is available only in the electronic edition.

Figure 6. Interferometric Synthetic Aperture Radar (InSAR) data and models of the mainshock deformation. The top two panels show observed ground deformation based (a) ascending and (b) descending directions. Focal mechanism plots denote the focal mechanism solutions from seismological data. Black line indicates the Molin fault. (c,d) The middle two represent coseismic model prediction, with the white rectangle denoting the source dimension and geometry. (e,f) The differences between the preferred model and observations. LoS, line of sight. The color version of this figure is available only in the electronic edition.

the Longmaxi formation of shale layer and thus the injection depth. However, the two foreshocks did not occur on the Molin fault, despite that their focal mechanisms were similar to that of the mainshock. To verify, we compared their waveforms on different stations with epicentral distances up to 100 km. The polarities of *P* waves appeared completely opposite at stations NZS and ROC (Fig. 5), which were at distances of 25 and 93 km, respectively. The *P*-wave polarities of the mainshock was positive at station NZS (azimuth of ∼160), whereas the two foreshocks showed downward motion. Such opposite first-motion polarities were also clear at station ROC (azimuth of ∼97), indicating different source faults of the mainshock and the foreshocks. In comparison, the two foreshocks had nearly identical waveforms across all stations (Fig. 5) and thus should occur on the same fault.

Constraints on the mainshock from InSAR data and modeling

Furthermore, we resolved the depth and rupture dimension of the mainshock using the Synthetic Aperture Radar (SAR) data.
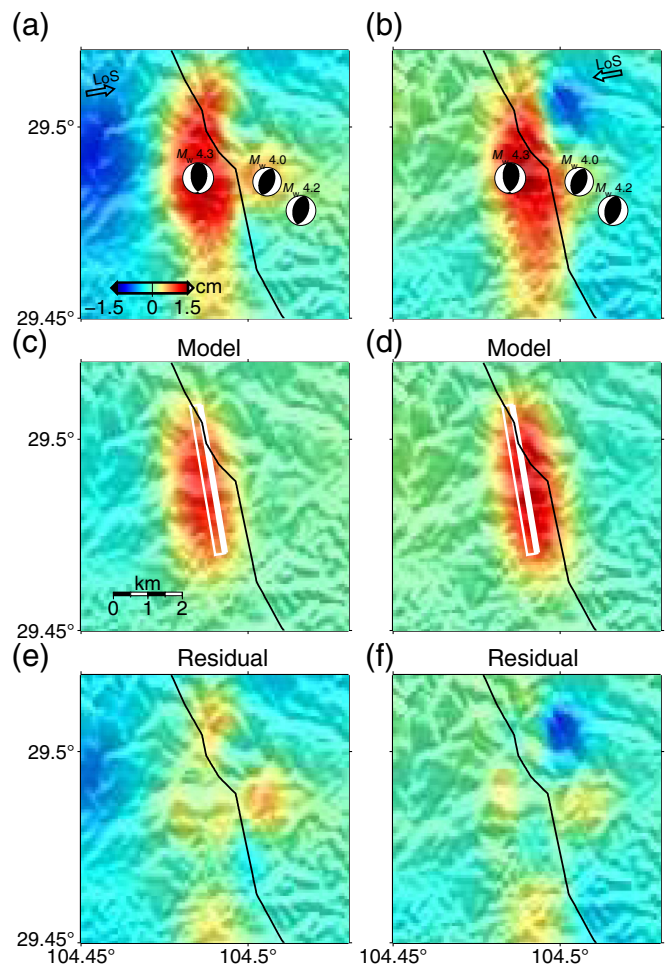
SAR images were acquired by European Space Agency's Sentinel-1 satellite, with one interferogram from an ascending orbit (14–26 February 2019) and the other from a descending track orbit (16–28 February 2019). Interferograms were formed using the GAMMA software, and the Shuttle Radar Topography Mission digital elevation models were used to remove the topographic effects. We used the minimum cost flow method to unwrap the two interferograms and then geocoded them into 1984 World Geodetic System (WGS84) coordinate system.

Two unwrapped interferograms from both ascending and descending orbit showed clear coseismic deformation up to 1.5 cm, consistent with thrust faulting on a nearly
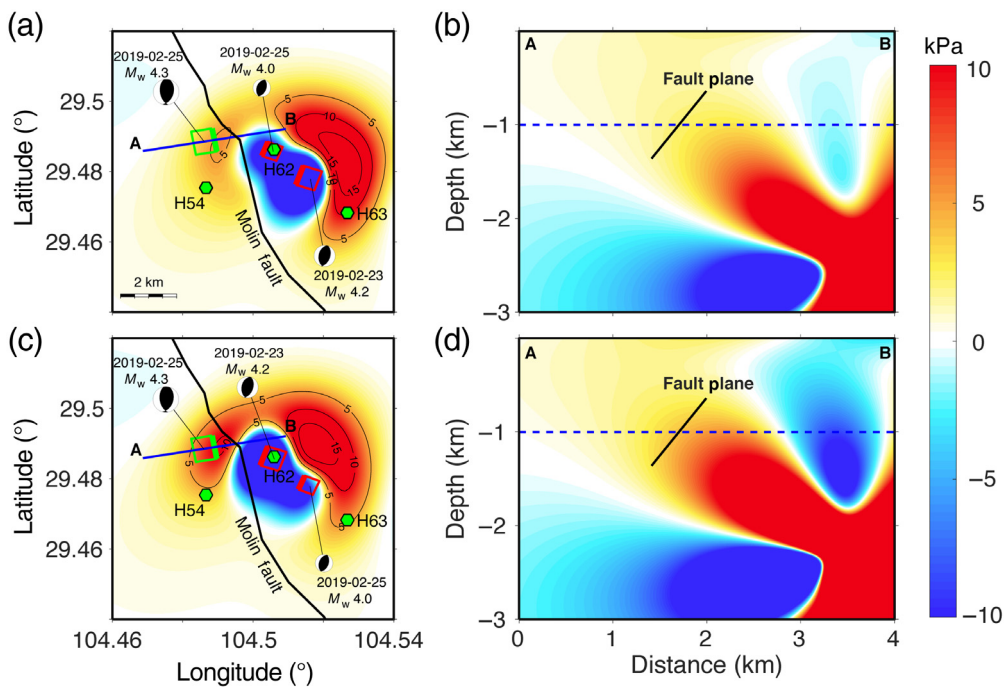
Figure 7. Coulomb failure stress (CFS) caused by the two foreshocks on receiver fault with the same geometry of the mainshock, which was assumed everywhere in the region. (a) Map view of the CFS (color) caused by the two foreshocks (red rectangles) on the mainshock fault (green rectangle). Contour lines denote 5 and 10 kPa, respectively. Nearby fracking well locations are shown by green hexagons. (b) CFS in the cross section whose location is shown in (a). (c) and (d) are same to (a) and (b), respectively, except for exchanging the locations of the two foreshocks. The color version of this figure is available only in the electronic edition.

north–south-striking fault (Fig. 6). Indeed, it was rare to observe ground deformation for earthquakes with such magnitude. We then retrieved the deformation source by geodetic inversion using a rectangular dislocation source in the half-space with Poisson's ratio $v = 0.25$ and shear modulus $\mu = 15$ GPa (Okada, 1992), which was defined by a fault plane position in space (strike, depth, dip, and coordinates of upper middle edge of fault), fault plane geometry (length and width), and the displacement components (strike-slip and dip-slip). We also conducted uncertainty estimation with a Bayesian method (see supplemental material) to form the posterior probability density function, with the moment magnitude determined by seismic data as the prior knowledge. For each of these inversion tests, we chose the best-fitting model that minimized the normalized root-mean-square error to the InSAR observations (Fig. S6; Table S1).

The best-fit model yielded an optimal moment magnitude 4.4 and a fault oriented 350° with a dip angle of 52° dipping to the west and a left-lateral slip in the direction 79°, remarkably consistent with the seismic solutions. Based on the Bayesian test (see supplemental material), distributions of each parameter showed that depth, strike, and the location of the fault were better constrained than the length, width, and slip of the fault

(Fig. S6). Parameters with uncertainties are listed in Table S1. From the Bayesian inference, the upper middle edge of the rectangular fault was located at latitude and longitude of (29.4919, 104.4779), with a buried depth of 1.33 km (Table 1), a length of 4.37 km and a width of 0.4 km (white rectangle in Fig. 6).

CFS caused by the two M 4+ foreshocks

We then calculated the static CFS changes (ΔCFS) caused by the two foreshocks on the mainshock's fault plane using Coulomb 3.4 software (Lin and Stein, 2004). The ΔCFS was defined as $\Delta\text{CFS} = \Delta\tau_s + \mu \times \Delta\sigma_n$, in which $\Delta\tau_s$ is the shear stress change (positive in the direction of receiver fault slip), $\Delta\sigma_n$ is the normal stress change (positive for extension), and μ is the effective fault friction coefficient (0.4 in this study). To focus on the potential triggering effects of the two **M** 4+ foreshocks on the mainshock, here we assumed the receiver fault geometry on each grid identical to the mainshock in the region. Using point-source parameters of the two foreshocks, we converted them into rectangle sources with uniform slip under the empirical scaling relationship. After calculation, we found that the mainshock fault plane had an increased ΔCFS of ∼3 kPa (Fig. 7a,b).

Although the location and depth of the mainshock were constrained by seismic and InSAR data, the two **M** 4+ foreshocks still had uncertainties up to ∼500 m in locations and depths. We thus considered the impact on calculated ΔCFS of location uncertainties by varying the depths and epicenters of the two foreshocks by 500 m (see supplemental material). The mainshock was always located in the area with positive ΔCFS (Fig. S7), with the peak value of ΔCFS less than 10 kPa. Because the two **M** 4+ foreshocks had nearly identical waveforms and should originate from the same fault, we tested an extreme case by exchanging their locations (Fig. 7c). As the M_w 4.2 foreshock moved closer to the mainshock, the value of ΔCFS increased to 7 kPa (Fig. 7c,d). As many outstanding observations indicated a minimal triggering stress of 10 kPa or higher (Stein, 1999), the two **M** 4+ foreshocks probably did not trigger the mainshock, despite the positive ΔCFS imparted on the mainshock fault plane.
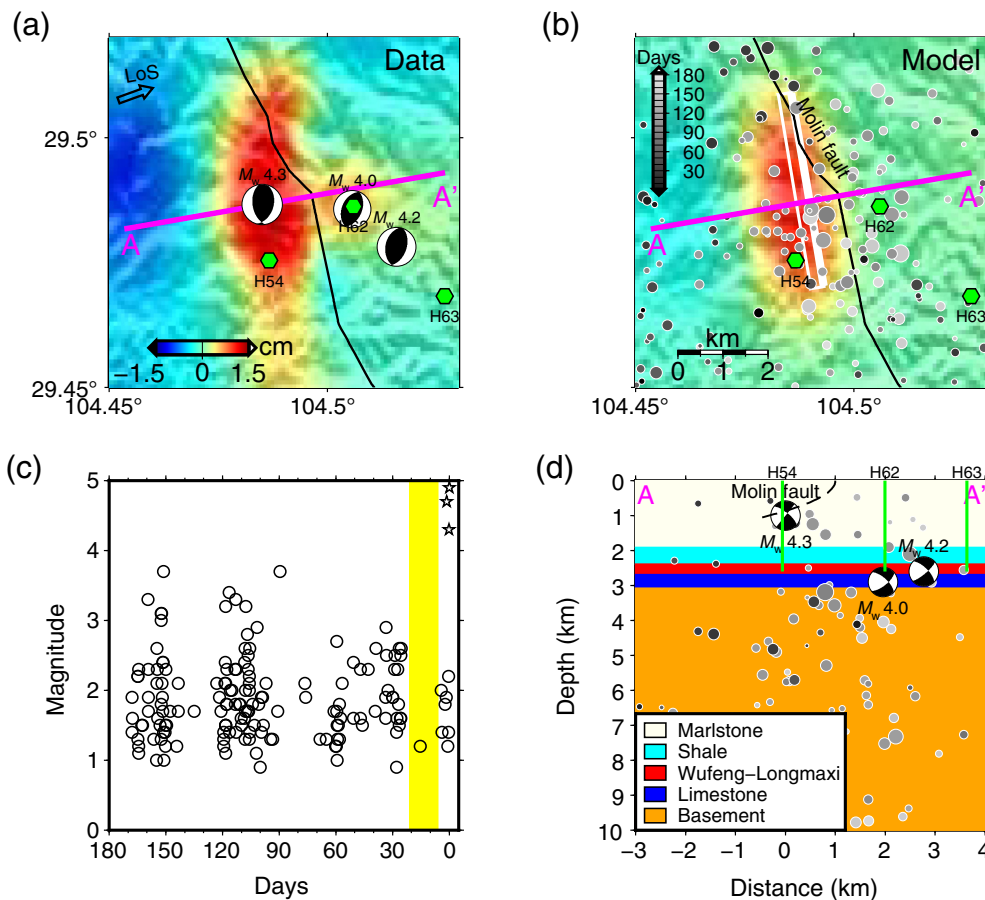
Figure 8. (a) Observed ground deformation (color) and moment tensor solutions from seismic data. Black line is the Molin fault. Green hexagons denote fracking wells. (b) Best-fit source model from InSAR data and seismicity (gray dots) in 180 days before the mainshock. A–A′ denotes a cross section shown in (d). (c) Local magnitude of seismicity (circles) before the three **M** 4+ earthquakes (stars). Yellow stripe denotes the holidays after the Spring Festival. (d) Seismicity, moment tensor solutions, Molin fault, and fracking wells projected on the cross section of A–A′. Background color denotes the simplified geological section (Dong et al., 2018). The color version of this figure is available only in the electronic edition.

Mechanism of the February 2019 Earthquake Sequence

The mainshock was preceded by numerous foreshocks, in addition to the two **M** 4+ ones nearby (Fig. 2b). However, most earthquakes were more than 5 km away from the Molin fault, on which the mainshock occurred (Fig. 2b). We first focused on the mainshock region, nearly twice of the mainshock rupture length (Fig. 8a). There were at least three fracking wells in this ~7 × 7 km^2 grid, with one located in the mainshock rupture zone and two within 2 km from the **M** 4+ foreshocks (Fig. 8a). Since September 2018, there had been a number of $M_L > 1$ earthquakes in the region, including two M_L 3.7 events (Fig. 8b,c). However, most of them occurred below 3 km in the basement formation and did not correlate with the Molin fault (Fig. 8d). The seismicity neither appeared to be spatially clustered nor exhibited clear migration pattern toward the mainshock or the two **M** 4+ foreshocks (Fig. 8b,d).

They did show temporal variations, however, with a few days with low or no seismicity (Fig. 8c). Around 20 days before the mainshock, there was a nearly two-week quiescence that corresponded to the holidays of Spring Festival dated on 5 February 2019. Although we did not have the accurate timing, wells H54 and H62 were in fracking operation before and after the break, for example, 19 February, and were all shut down after the mainshock occurrence on 25 February. The two **M** 4+ foreshocks were located at ~2.6–2.9 km in depth and had nearly identical waveforms, indicating that they originated from the same fault. The injection well, H62, is located exactly at the hypocenter of the M_w 4.0 earthquake; whereas the other well (H63) is within 1 km from the epicenter of the M_w 4.2 event. As such, we interpreted that these two **M** 4+ earthquakes were induced by fracking. Potential mechanisms included pore-pressure perturbation, poroelastic stress transfer, and/or aseismic slip triggered by fluid injection. Because of the lack of accurate injection data and seismicity migration, we cannot distinguish these mechanisms.

The mainshock, however, was located at 1 km in depth within the marlstone layer (Fig. 8d), well above the Longmaxi shale formation. According to results of laboratory frictional experiments on sedimentary rock samples (mudstone, sandstone, and limestone) from the Longmen Shan fault zone, all samples under conditions representing shallow depths (<2 km) exhibited velocity strengthening (VS) behavior (Verberne et al., 2010). Although a VS patch was normally anticipated to slip aseismically, it may break during earthquake ruptures because of strong loading from neighboring segment (Yang et al., 2012). In this case, potential sources of loading and consequently inducing coseismic slip on the Molin fault included the following: pore-fluid pressure increase on the fault plane due to the fracking fluid injection; aseismic slip triggered by fluid injection on the fault; static stress exerted from

the two **M** 4+ foreshocks; and poroelastic stress perturbation due to fluid injection.

Although there was a fracking well (H54) in the mainshock ruptured zone (Fig. 8a), the injection depth is ~2.7 km at the Longmaxi formation, at least 1.7 km deeper than the focal depth of the mainshock. Because there is another shale layer of ~800 m in thickness atop the Wufeng–Longmaxi formation (Fig. 8d), fracking fluids presumably cannot migrate upward into the Molin fault. Therefore, the Molin fault should not hydraulically connect with the injected fluids, and thus pore-pressure elevation would be unlikely. Indeed, the Molin fault ceased at depth of ~1 km on the detachment and did not extend to the depth of injection. As such, it was not feasible to have injection-induced aseismic slip propagating into shallower depth and generating the mainshock, as suggested by observations in central Alberta, Canada (Eyre et al., 2019).

Because the ΔCFS from the two foreshocks was rather small, and pore-pressure diffusion and injection-induced aseismic slip were unlikely, poroelastic stress associated with HF was plausible to trigger the mainshock occurrence on the Molin fault that was supposed to be stable. Indeed, poroelastic stress changes had been suggested to impact fault reactivation in distances (e.g., Chang and Segall, 2016; Jiang et al., 2020). In a 2D numerical model, the poroelastic stress induced ΔCFS on basement faults that were hydraulically sealed and 1 km beneath the injection zone reached the order of 100 kPa (Chang and Segall, 2016). In the Changning region, the calculated ΔCFS on basement faults due to poroelastic stress changes was ~100 kPa for one single injection well (Lei et al., 2017). Considering hydraulically sealed faults above or at the same depth of injection, the ΔCFS can reach at least 10 kPa in a distance of 2.5 km, even for injected natural gas that has smaller density and compressibility than liquid (Jiang et al., 2020). Although we did not develop a geomechanics model in this study, because we do not have the injection data, the estimated values of ΔCFS due to poroelastic stress was likely on the order similar to reports in the Changning region (i.e., 100 kPa), much larger than the ΔCFS caused by the two **M** 4+ foreshocks (3 kPa). Quantitative modeling with operational data is encouraged and shall be conducted if the injection data become available.

Discussion

Unlike in the central United States, where wastewater disposal significantly affected seismicity with larger footprints and longer time periods (Ellsworth, 2013; Goebel et al., 2017), wastewater disposal was not significant in the Sichuan basin, because most of them had been reused for fracking (Lei et al., 2017, 2019a). Thus, most induced earthquakes in the shale gas field of Sichuan basin were suggested to relate with fracking (Lei et al., 2017, 2019a; Meng et al., 2019). Fracking effect was suggested to be localized in both horizontal and vertical

distances to the injection zones (e.g., Davies et al., 2012; Flewelling et al., 2013; Deng et al., 2016; Yu et al., 2019), and, thus it should be of paramount importance in seismic hazard mitigation, when injection sites were projected near preexisting faults.

An imperative strategy was to limit injection near known faults that are preferentially oriented to fail in the regional stress field. However, lots of induced earthquakes occurred on unknown faults that were only detected after earthquakes (e.g., Rubinstein et al., 2014). In the February 2019 Rongxian–Weiyuan sequence, the **M** 4+ foreshocks occurred on an unmapped fault orienting northeast that was activated by fracking, demonstrating the difficulty in forecasting and preventing damaging earthquakes due to our incomplete knowledge of subsurface structures (Yeck et al., 2017). Densified seismic network was important to capture microseismicity, so as to derive their spatial and temporal evolution, which was helpful to delineate such faults. In the Rongxian–Weiyuan region, seismic stations before the mainshock were in distances greater than 15 km from the epicenters, limiting the network detection of small earthquakes and location resolution. A mobile seismic network was deployed, a few days after the mainshock, to record aftershocks. In the future, more permanent seismic stations in the region will be needed to elucidate the causal relationship between seismicity and fracking activities.

Most HF-induced earthquakes were found to nucleate on faults beneath the injection depth (Bao and Eaton, 2016; Lei et al., 2017; Skoumal et al., 2018). In the Changning region, where M_w 5+ earthquakes were suggested to be triggered by HF (Lei et al., 2019a), the majority of earthquakes occurred at depths 2–6 km. In our study area, most seismicity including the two **M** 4+ events also occurred no shallower than the fracking depth (~2.7 km). However, the mainshock was extremely shallow, 1 km below the ground, on the Molin fault that was previously mapped by geological survey (Wei et al., 2008). The real surprise was that the Molin fault did not extend greater than ~1.5 km at depth, and merged with the detachment layer according to 3D seismic reflection profiles. Both observations of tectonic earthquakes and results of frictional experiments suggested that a fault at such shallow depth would have been usually considered stable and thus would not anticipate earthquakes (Scholz, 1998). The 25 February 2019 M_L 4.9 earthquake apparently posed challenges on such traditional view and how to evaluate potential seismic hazard and risks for injections near very shallow faults.

Compared with the southern fold zone in the Sichuan basin, for example, Changning region, where earthquakes with magnitudes up to 6 had occurred (Lei et al., 2019b), the Rongxian–Weiyuan region had been speculated less likely to generate **M** 4 earthquakes (Lei et al., 2017), because of weaker sediment deformations and fewer identified faults in the basement. However, the Rongxian–Weiyuan earthquakes changed our

views on the potential magnitudes of earthquakes in the region. Indeed, on 8 September 2019, an M_w 5.4 earthquake occurred in the Weiyuan County and claimed one death and more than 60 injuries (M. Sheng *et al.*, unpublished manuscript, 2020, see Data and Resources). Another M_L 4.3 earthquake occurred on the same day, very close to the epicenters of the February earthquakes, demonstrating the urgent need to better evaluate seismic hazard in the Sichuan basin for purposes of mitigating their effects. The large population and aging infrastructure in the region made it even more vulnerable when earthquakes with similar or larger magnitudes occurred (Lei *et al.*, 2017, 2019a). However, transparency of industrial data was invaluable to better evaluating risks of potential induced earthquakes (McGarr *et al.*, 2015). Given the ambitious plan of natural gas in China, it is necessary to promote collaborations among different stakeholders, such as regulators, operators, and the scientific community to make correct and timely decisions, aiming at sustainable shale gas development (Lei *et al.*, 2017; Yang *et al.*, 2017).

Conclusions

We conducted a detailed analysis using both seismic and geodetic data on the February 2019 Rongxian–Weiyuan earthquake sequence. Most of these earthquakes occurred at 2–6 km in depth, with the M_w 4.0 and 4.2 foreshocks at ∼3 km, coinciding with the depth where fracking was conducted. The two foreshocks ruptured an unmapped fault that was reactivated by fracking. The M_L 4.9 (M_w 4.3) earthquake occurred at extremely shallow depth, 1 km below the surface, one of the reasons to cause destructive damage. As the Molin fault was hydraulically sealed from injection activities, pore-pressure elevation and injection-induced aseismic slip were thus unlikely to be the triggering mechanisms for the mainshock. CFS caused by the two foreshocks was positive yet smaller than the typical threshold (10 kPa) suggested to trigger seismicity. Therefore, we suggested that the Rongxian–Weiyuan earthquake was plausibly induced by HF through poroelastic stress transfer onto the Molin fault that was supposed to be aseismic at the shallow depth.

Data and Resources

Earthquake catalog was obtained from the China Earthquake Data Center (CEDC, http://data.earthquake.cn/index.html, last accessed August 2020). Seismic waveform data used in this study were requested with a preauthorized account from Data Management Centre of China Seismic Network (doi: 10.1785/0120090257). Phase data were from Sichuan Earthquake Agency. Synthetic Aperture Radar (SAR) images were acquired by European Space Agency's Sentinel-1 satellite. Well locations were compiled from reports listed in local government website http://www.weiyuan.gov.cn/news/show?id=143709 (last accessed July 2020). Information of fatality and damage was reported by The Paper (https://www.thepaper.cn/newsDetail_forward_3038167, last accessed April 2019). Supplemental material

for this article includes additional details of analyses and the catalog of relocated earthquakes. The unpublished manuscript by M. Sheng, R. Chu, S. Ni, Y. Wang, L. Jiang, and H. Yang (2020), "Source parameters of three moderate-size induced earthquakes at the Weiyuan shale gas field in southwestern China," submitted to *J. Geophys. Res.*

References

Atkinson, G. M., D. W. Eaton, H. Ghofrani, D. Walker, B. Cheadle, R. Schultz, R. Shcherbakov, K. Tiampo, J. Gu, R. M. Harrington, *et al.* (2016). Hydraulic fracturing and seismicity in the Western Canada Sedimentary Basin, *Seismol. Res. Lett.* **87,** no. 3, 631–647, doi: 10.1785/0220150263.

Babaie Mahani, A., H. Kao, G. M. Atkinson, K. Assatourians, K. Addo, and Y. Liu (2019). Ground motion characteristics of the 30 November 2018 injection-induced earthquake sequence in northeast British Columbia, Canada, *Seismol. Res. Lett.* **90,** no. 4, 1457–1467.

Bao, X., and D. W. Eaton (2016). Fault activation by hydraulic fracturing in western Canada, *Science* **354,** no. 6318, 1406–1409, doi: 10.1126/science.aag2583.

Bhattacharya, P., and R. C. Viesca (2019). Fluid-induced aseismic fault slip outpaces pore-fluid migration, *Science* **364,** 464–468.

Brown, M. R. M., and S. Ge (2018). Small earthquakes matter in injection-induced seismicity, *Geophys. Res. Lett.* **45,** 5445–5453, doi: 10.1029/2018GL077472.

Chang, K. W., and P. Segall (2016). Injection induced seismicity on basement faults including poroelastic stressing, *J. Geophys. Res.* **121,** doi: 10.1002/2015JB012561.

Clarke, H., L. Eisner, P. Styles, and P. Turner (2014). Felt seismicity associated with shale gas hydraulic fracturing: The first documented example in Europe, *Geophys. Res. Lett.* **41,** 8308–8314, doi: 10.1002/2014GL062047.

Davies, R. J., S. A. Mathias, J. Moss, S. Hustoft, and L. Newport (2012). Hydraulic fractures: How far can they go? *Mar. Petrol. Geol.* **37,** no. 1, 1–6, doi: 10.1016/j.marpetgeo.2012.04.001.

Deng, K., Y. Liu, and R. M. Harrington (2016). Poroelastic stress triggering of the December 2013 Crooked Lake, Alberta, induced seismicity sequence, *Geophys. Res. Lett.* **43,** 8482–8491, doi: 10.1002/2016GL070421.

Dong, D., Z. Shi, Q. Guang, S. Jiang, M. Zhang, C. Zhang, S. Wang, S. Sun, R. Yu, D. Liu, *et al.* (2018). Progress, challenges and prospects of shale gas exploration in the Wufeng–Longmaxi reservoirs in the Sichuan Basin, *Nat. Gas Ind.* **38,** no. 4, 67–76 (in Chinese).

Ellsworth, W. L. (2013). Injection-induced earthquakes, *Science* **341,** no. 6142, 1225942, doi: 10.1126/science.1225942.

Ellsworth, W. L., D. Giardini, J. Townend, S. Ge, and T. Shimamoto (2019). Triggering of the Pohang, Korea, earthquake (M_w 5.5) by enhanced geothermal system stimulation, *Seismol. Res. Lett.* **90,** no. 5, doi: 10.1785/0220190102.

Eyre, T. S., D. W. Eaton, D. I. Garagash, M. Zecevic, M. Venieri, R. Weir, and D. C. Lawton (2019). The role of aseismic slip in hydraulic fracturing-induced seismicity, *Sci. Adv.* **5,** eaav7172.

Flewelling, S. A., M. P. Tymchak, and N. Warpinski (2013). Hydraulic fracture height limits and fault interactions in tight oil and gas formations, *Geophys. Res. Lett.* **40,** 3602–3606, doi: 10.1002/grl.50707.

Goebel, T. H. W., M. Weingarten, X. Chen, J. Haffener, and E. E. Brodsky (2017). The 2016 M_w 5.1 Fairview, Oklahoma earthquakes: Evidence for long-range poroelastic triggering at >40 km from fluid disposal wells, *Earth Planet. Sci. Lett.* **472,** 50–61.

Grigoli, F., S. Cesca, E. Priolo, A. P. Rinaldi, J. F. Clinton, T. A. Stabile, B. Dost, M. G. Fernandez, S. Wiemer, and T. Dahm (2017). Current challenges in monitoring, discrimination, and management of induced seismicity related to underground industrial activities: A European perspective, *Rev. Geophys.* **55,** no. 2, 310–340, doi: 10.1002/2016RG000542.

Grigoli, F., S. Cesca, A. P. Rinaldi, A. Manconi, J. A. Lopez-Comino, J. F. Clinton, R. Westaway, C. Cauzzi, T. Dahm, and S. Wiemer (2018). The November 2017 M_w 5.5 Pohang earthquake: A possible case of induced seismicity in South Korea, *Science* **360,** no. 6392, 1003–1006, doi: 10.1126/science.aat2010.

Jiang, G., X. Qiao, X. Wang, R. Lu, L. Liu, H. Yang, Y. Su, L. Song, B. Wang, and T. Wong (2020). GPS observed horizontal ground extension at the Hutubi (China) underground gas storage facility and its application to geomechanical modeling for induced seismicity, *Earth Planet. Sci. Lett.* **530,** 115943.

Kim, K.-H., J.-H. Ree, Y. Kim, S. Kim, S. Y. Kang, and W. Seo (2018). Assessing whether the 2017 M_w 5.4 Pohang earthquake in South Korea was an induced event, *Science* **360,** 1007–1009, doi: 10.1126/science.aat6081.

Lei, X., D. Huang, J. Su, G. Jiang, X. Wang, H. Wang, X. Guo, and H. Fu (2017). Fault reactivation and earthquakes with magnitudes of up to Mw 4.7 induced by shale-gas hydraulic fracturing in Sichuan Basin, China, *Sci. Rep.* **7,** 7971, doi: 10.1038/s41598-017-08557-y.

Lei, X., Z. Wang, and J. Su (2019a). The December 2018 M_L 5.7 and January 2019 M_L 5.3 earthquakes in South Sichuan Basin induced by shale gas hydraulic fracturing, *Seismol. Res. Lett.* **90,** no. 3, doi: 10.1785/0220190029.

Lei, X., Z. Wang, and J. Su (2019b). Possible link between long-term and short-term water injections and earthquakes in salt mine and shale gas site in Changning, south Sichuan Basin, China, *Earth Planet. Phys.* **3,** 510–525, doi: 10.26464/epp2019052.

Lin, J., and R. S. Stein (2004). Stress triggering in thrust and subduction earthquakes and stress interaction between the southern San Andreas and nearby thrust and strike-slip faults, *J. Geophys. Res.* **109,** doi: 10.1029/2003JB002607.

Ma, C., X. Zhang, and S. Li (2017). 3D geological modeling of effective shale-gas reservoirs: Taking Wei 202H2 platform of Weiyuan area as an example, *Fault Block Oil Gas Field* **24,** no. 4, 495–499, doi: 10.6056/dkyqt201704013 (in Chinese).

McGarr, A., B. Bekins, N. Burkardt, J. Dewey, P. Earle, W. Ellsworth, S. Ge, S. Hickman, A. Holland, E. Majer, *et al.* (2015). Coping with earthquakes induced by fluid injection, *Science* **347,** no. 6224, 830–831.

Meng, L., A. McGarr, L. Zhou, and Y. Zang (2019). An investigation of seismicity induced by hydraulic fracturing in the Sichuan Basin of China based on data from a temporary seismic network, *Bull. Seismol. Soc. Am.* **109,** no. 1, 348–357, doi: 10.1785/0120180310.

Meng, X., H. Chen, F. Niu, and Y. Tang (2018). Microseismic monitoring of stimulating shale gas reservoir in SW China: 1. An improved match and locate technique for downhole monitoring, *J. Geophys. Res.* **123,** doi: 10.1002/2017JB014488.

Okada, Y. (1992). Internal deformation due to shear and tensile faults in a half-space, *Bull. Seismol. Soc. Am.* **82,** 1018–1040.

Rubinstein, J. L., W. L. Ellsworth, A. McGarr, and H. M. Benz (2014). The 2001-present induced earthquake sequence in the Raton Basin of Northern New Mexico and Southern Colorado, *Bull. Seismol. Soc. Am.* **104,** no. 5, 2162–2181.

Scholz, C. H. (1998). Earthquakes and friction laws, *Nature* **391,** 37–42.

Skoumal, R. J., R. Ries, M. R. Brudzinski, A. J. Barbour, and B. S. Currie (2018). Earthquakes induced by hydraulic fracturing are pervasive in Oklahoma, *J. Geophys. Res.* **123,** doi: 10.1029/2018JB016790.

Stein, R. (1999). The role of stress transfer in earthquake occurrence, *Nature* **402,** 605–609.

Verberne, B. A., C. He, and C. J. Spiers (2010). Frictional properties of sedimentary rocks and natural fault gouge from the Longmen Shan fault zone, Sichuan, China, *Bull. Seismol. Soc. Am.* **100,** no. 5B, 2767–2790, doi: 10.1785/0120090287.

Waldhauser, F., and W. L. Ellsworth (2000). A double-difference earthquake location algorithm: Method and application to the Northern Hayward Fault, California, *Bull. Seismol. Soc. Am.* **90,** no. 6, 1353–1368, doi: 10.1785/0120000006.

Wang, B., R. M. Harrington, Y. Liu, H. Kao, and H. Yu (2020). A Study on the largest hydraulic-fracturing-induced earthquake in Canada: Observations and static stress-drop estimation, *Bull. Seismol. Soc. Am.* doi: 10.1785/0120190261.

Wang, M., H. Yang, L. Fang, L. Han, D. Jia, D. Jiang, and B. Yan (2020). Shallow fault activation induced by hydraulic fracturing: The 2019 Weiyuan earthquake sequences in Sichuan, China, *Seismol. Res. Lett.* doi: 10.1785/0220200174.

Wang, X., S. Ma, Z. Guo, X. Lei, Y. Xia, X. Guo, G. Yu, X. Gou, X. Jiang, *et al.* (2013). S-wave velocity of the crust in Three Gorges Reservoir and the adjacent region inverted from seismic ambient noise tomography, *Chin. J. Geophys.* **56,** no. 12, doi: 10.6038/cjg20131216 (in Chinese).

Wei, G., G. Chen, S. Du, L. Zhang, and W. Yang (2008). Petroleum systems of the oldest gas field in China: Neoproterozoic gas pools in the Weiyuan gas field, Sichuan Basin, *Mar. Petrol. Geol.* **25,** nos. 4/5, 371–386, doi: 10.1016/j.marpetgeo.2008.01.009.

Wu, X., J. Xia, B. Guan, X. Yan, L. Zou, P. Liu, L. Yang, S. Hong, and S. Hu (2019). Water availability assessment of shale gas production in the Weiyuan Play, China, *Sustainability* **11,** no. 3, 940, doi: 10.3390/su11030940.

Yang, H., Y. Liu, and J. Lin (2012). Effects of subducted seamounts on megathrust earthquake nucleation and rupture propagation, *Geophys. Res. Lett.* **39,** no. 24, doi: 10.1029/2012GL053892.

Yang, H., Y. Liu, M. Wei, J. Zhuang, and S. Zhou (2017). Induced earthquakes in the development of unconventional energy resources, *Sci. China Earth Sci.* **60,** no. 9, 1632–1644, doi: 10.1007/s11430-017-9063-0.

Yeck, W. L., G. P. Hayes, D. E. McNamara, J. L. Rubinstein, W. D. Barnhart, P. S. Earle, and H. M. Benz (2017). Oklahoma experiences largest earthquake during ongoing regional wastewater injection hazard mitigation efforts, *Geophys. Res. Lett.* **44,** 711–717, doi: 10.1002/2016GL071685.

Yu, H., R. M. Harrington, Y. Liu, and B. Wang (2019). Induced seismicity driven by fluid diffusion revealed by a near-field hydraulic stimulation monitoring array in the Montney Basin, British Columbia, *J. Geophys. Res.* **124,** doi: 10.1029/2018JB017039.

Zhao, Z., J. Fan, S. Zheng, A. Hasegawa, and S. Horiuchi (1997). Precision determination of the crustal structure and hypocentral locations in the Longmenshan thrust nappe belt, *Acta Seismol. Sin.* **19,** no. 6, 6l5–622 (in Chinese).

Zheng, X., Z. Yao, J. Liang, and J. Zheng (2010). The role played and opportunities provided by IGP DMC of China National Seismic Network in Wenchuan earthquake disaster relief and researches, *Bull. Seismol. Soc. Am.* **100,** no. 5B, 2866–2872, doi: 10.1785/0120090257.

Zhou, P., H. Yang, B. Wang, and J. Zhuang (2019). Seismological investigations of induced earthquakes near the Hutubi underground gas storage facility, *J. Geophys. Res.* **124,** doi: 10.1029/2019JB017360.

Zhu, L., and Y. Ben-Zion (2013). Parameterization of general seismic potency and moment tensors for source inversion of seismic waveform data, *Geophys. J. Int.* **194,** 839–843, doi: 10.1093/gji/ggt137.

Zhu, L., and D. Helmberger (1996). Advancement in source estimation techniques using broadband regional seismograms, *Bull. Seismol. Soc. Am.* **86,** no. 5, 1634–1641.

Zhu, L., and L. A. Rivera (2002). A note on the dynamic and static displacements from a point source in multilayered media, *Geophys. J. Int.* **148,** no. 3, 619–627, doi: 10.1046/j.1365-246X.2002.01610.x.